Check for updates

Identifying Shocked Feldspar on Mars Using Perseverance Spectroscopic Instruments: Implications for Geochronology Studies on Returned Samples

S. Shkolyar[1,2,3] · S. J. Jaret[4] · B. A. Cohen[2] · J. R. Johnson[5] · O. Beyssac[6] ·
J. M. Madariaga[7] · R. C. Wiens[8] · A. Ollila[8] · S. Holm-Alwmark[9,10,11] · Y. Liu[12]

© The Author(s), under exclusive licence to Springer Nature B.V. 2022

Abstract

The *Perseverance* rover (Mars 2020) mission, the first step in NASA's Mars Sample Return (MSR) program, will select samples for caching based on their potential to improve understanding Mars' astrobiological, geological, geochemical, and climatic evolution. Geochronologic analyses will be among the key measurements planned for returned samples. Assessing a sample's shock history will be critical because shock metamorphism could influence apparent sample age. Shock effects in one Mars-relevant mineral class, plagioclase feldspar, have been well-documented using various spectroscopy techniques (thermal infrared reflectance, emission, and transmission spectroscopy, Raman, and luminescence). A subset of these data will be obtained with the SuperCam and SHERLOC (Scanning Habitable Environments with Raman & Luminescence for Organics & Chemicals) instruments onboard *Perseverance* to inform caching decisions for MSR. Here, we review shock indicators in plagioclase feldspar as revealed in Raman, luminescence, and IR spectroscopy lab data, with an emphasis on Raman spectroscopy. We consider how this information may inform caching decisions for selecting optimal samples for geochronology measurements. We then identify challenges and make recommendations for both in situ measurements performed with SuperCam and SHERLOC and for supporting lab studies to enhance the success of geochronologic analyses after return to Earth.

Keywords Mars sample return · Spectroscopy · Perseverance rover

1 Introduction

The Mars Sample Return (MSR) Program is NASA's first attempt to perform in situ characterization of samples collected and cached on the surface of Mars for later return to Earth and analysis in state-of the-art laboratories. The first step of MSR is being fulfilled by the *Perseverance* rover (Mars 2020 mission), which landed on Mars on February 18, 2021, and is currently active in the selected landing site, Jezero crater. Jezero, located at the western

---

✉ S. Shkolyar
    svet@bmsis.org

Extended author information available on the last page of the article

edge of the Isidis basin, contains considerable lithological diversity, including units that may have been formed in deltaic or fluvial settings that may have constituted habitable environments (Ehlmann et al. 2008a; Williford et al. 2018; Goudge et al. 2015; Farley et al. 2020; Stack et al. 2020). Jezero lithologies will be investigated with instruments onboard *Perseverance* and prioritized for cache and Earth return based on their potential to characterize the geologic history and evolution of Mars, including those that that reveal habitable environments and potential biosignatures, record Mars' past geochemical evolution, and constrain the longevity of these geologic settings.

This review focuses on informing strategies to achieve the latter goal, and more specifically, to inform the selection of samples for geochronologic analyses on Earth. We explore how impact metamorphism may affect geochronology analyses of returned samples and the extent to which shock-altered materials can be identified on Mars using spectroscopy instruments onboard *Perseverance*. We then identify major challenges and make recommendations for spectroscopy analyses onboard *Perseverance* as well as for supporting lab studies, both of which may optimize the selection of samples for geochronologic analyses on Earth.

1.1 The Geochronology of Mars and Jezero Crater

A longstanding goal of the Mars Exploration Program has been to understand the timing of different geologic processes as the planet has evolved, identified as a major driver of sample return by multiple reports (MEPAG ND-SAG 2008; McLennan et al. 2012; Mustard et al. 2013; Beaty et al. 2019; MASWG 2020; NASA 2020). An improved understanding of geochronology has the potential to place Martian climate change into the context of Martian evolution and solar system history (Doran et al. 2004; Cohen et al. 2019).

Our current understanding of Mars chronology is based on absolute ages (and supporting measurements) on the Martian meteorite suite, stratigraphic relationships of geologic units on the Martian surface, and in situ dating on the Mars Science Laboratory mission, but at present, there are not any large-scale Martian terrains that can be tied to absolute radiometric dates to extend our understanding of Martian geochronology planetwide (Tanaka 1986; Farley et al. 2014; Grady 2020). Measurements from meteorites show that Mars accreted early in the solar system from materials with an isotopic provenance distinct from the Earth-Moon system (Dauphas and Pourmand 2011; Warren 2011). Mars formed a magma ocean within ~ 100 Ma after solar system formation and then differentiated into a crust, mantle, and core (Debaille et al. 2007). Most of the mass of the Martian crust formed by ~ 4.35 Ga, but substantial crust may have cooled and solidified earlier to support the formation of the Borealis basin very early on Martian history (Humayun et al. 2013). An epoch of Late Heavy Bombardment, similar to that proposed for the Moon and asteroid belt, probably affected Mars at around 4.1 Ga, creating the Isidis, Hellas and Argyre basins (Bottke and Andrews-Hanna 2017; Cohen 2006). Magmatism has been active over most of Martian geologic history, as shown by the relatively young ages of shergottites and nakhlites (on the order of Ma with most around 350 Ma; Nyquist et al. 2009).

Using relative stratigraphy to understand planetwide Martian chronology is based on assumptions derived from lunar crater size-frequency relationships correlated to laboratory-dated, returned lunar samples (Neukum et al. 2001; Stöffler and Ryder 2001; Cohen et al. 2019). These assumptions include uncertainties anywhere from a factor of 2 or up to a billion years, depending on estimated impact fluxes and crater counting techniques (Hartmann and Neukum 2001; Bottke and Norman 2017). Additional uncertainty comes from

volcanic, fluvial and/or aeolian weathering that can degrade and erase impact craters on Mars (Tanaka 1986; Hartmann 1999).

The Mars Science Laboratory (MSL) rover demonstrated radiometric dating techniques within Gale Crater, making K–Ar measurements of the detrital minerals in the Sheepbed mudstone (Farley et al. 2014) and dating the time of fluid infiltration in the Mojave 2 mudstone (Martin et al. 2017). However, these measurements were not precise enough to cross-calibrate the Martian crater density record with radiometric ages across the whole planet (Cohen et al. 2019).

In situ radiometric dating techniques on planetary surfaces hold promise for constraining geochronology on Mars. A review of flight techniques for geochronology studies currently in development can be found in Cohen et al. (2019) and references therein. However, until in situ geochronology instruments are flown in a mission, the most accurate age measurements are likely to be obtained on samples returned to the Earth from Mars (Stipe et al. 2012).

Multiple lithologic units within Jezero crater have the potential to place stronger constraints on the timing of Martian geologic events when samples are returned to terrestrial laboratories (e.g., Beaty et al. 2019; Farley et al. 2020). The Jezero crater floor is largely covered by a unit with mafic mineralogy and greater impact crater retention than other bedrock exposed in Jezero, though the origin of the unit as volcanic or sedimentary is not yet established (Goudge et al. 2015; Rogers et al. 2018; Shahrzad et al. 2019). For a variety of reasons explored by Shahrzad et al. (2019), three different ages have been estimated for this unit based on its observed crater size-frequency distribution: 1.4 Ga (Schon et al. 2012), 2.5 Ga (Shahrzad et al. 2019; Rubanenko et al. 2021), and 3.5 Ga (Goudge et al. 2012). The wide range of apparent ages hinders interpretations of the Jezero crater formation age and subsequent floor filling events, but precise radiometric ages on returned samples may help determine a crystallization age that would be relatable to the Martian crater flux function, or the formation and exposure age of its detrital precursors. Jezero crater also contains an olivine-carbonate assemblage that may be similar to carbonate and olivine-bearing light-toned fractured rocks around the inner rim of Jezero crater and extend outside the crater rim in Nili Fossae (Ehlmann et al. 2008b; Brown et al. 2020; Horgan et al. 2020). A crater density age of 3.82 ± 0.07 Ga has been estimated for the Nili Fossae olivine-carbonate unit (Mandon et al. 2020). Laboratory-determined ages of this unit would not only place important constraints on its origin but may also help establish an absolutely-dated stratigraphic horizon well beyond Jezero. Finally, the Jezero delta unit may be the best unit to contain potential biosignatures and a past habitable environment. The deltaic/lacustrine deposit on the Jezero floor reveals remote-sensing evidence of hydrothermal alteration products, including clays and carbonates (Brown et al. 2010; Schon et al. 2012; Goudge et al. 2015), some of which may be directly datable to provide precise knowledge of when the delta was deposited and how long fluvial activity continued.

1.1.1 Understanding Shock Effects in Returned Martian Samples for Geochronology

To best prioritize samples for caching and for geochronology analyses on returned samples, it will be crucial to assess their degree of alteration and understand how their isotopic systems may have been affected by secondary processes. On Earth as well as Mars, geochronologists need to consider secondary processes overprinting original crystallization ages,

since post-crystallization heating events (e.g., burial or metamorphism), aqueous alteration, and shock disturbance can disturb or reset isotopic systems.

Robustness to impact events varies by chronometer and phase; the same impact-affected rock can yield different ages by different chronometers (e.g., Schärer et al. 1990; Jourdan et al. 2009; Jourdan 2012; Jaret et al 2018b, Schmieder et al. 2020). Multiple relevant dating methods may be desirable on a single sample to allow an internal cross-check on age interpretations performed in terrestrial labs. Multiple geochemical and contextual measurements would be possible with a single sample core (~ 15 g) cached on Mars and returned to Earth. For this review, we focus specifically on recognizing shock effects in feldspar, most commonly dated using the K–Ar system (e.g. McDougall and Harrison 1999). While other chronometers and minerals (e.g., U–Pb in zircon or apatite) are undoubtedly useful (e.g., Cavosie et al. 2015; Erickson et al. 2017; Kenny et al. 2017), the effects of shock in these systems and how they would be recognized with the Perseverance rover are topics of further study. Nevertheless, the ability to recognize shock effects in a single mineral would set a reasonable expectation that other minerals in the same rock may have been affected by shock pressures that could potentially influence the results from other isotopic systems.

1.1.2 Analyses Favoring Minimally Shock-Altered Samples

One process that could hamper geochronology analyses is high pressures or temperatures associated with impact cratering. Shock metamorphic effects are known from impact craters on Earth, from returned lunar samples, and in meteorites (from Mars, Vesta, and asteroids; Stöffler et al. 2018). Hypervelocity impact events are extreme in terms of energy release, pressures, temperatures, and strain rates (e.g., Melosh 1989). Minerals develop shock metamorphic effects as a response to the passing shock wave during impact, and that response differs based on mineral type and shock level. For plagioclase feldspars, these effects are summarized in Fig. 1.

Impact-induced shock and deformation of geological materials can disturb isotopic systems such as Ar–Ar and U–Pb (e.g., Jourdan et al. 2009; Jourdan 2012; Jaret et al. 2018b; McGregor et al. 2018). Impact metamorphism combines the effects of shock
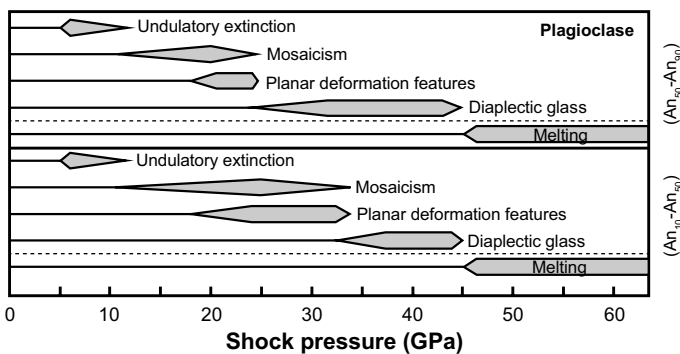

Fig. 1 Shock effects in different types of plagioclase feldspars. Note that diagram only shows effects with increasing pressure (x-axis). After Stöffler et al. (2018). While shock states here are based on the Stöffler classification scheme, an optical petrographic classification, note that this is meant to be a guide of general shock state. In some cases, linking this traditional and standard optical classification with spectroscopic classification can be challenging as optics and spectroscopy can probe different modes of feldspar disordering (Jaret et al. 2018a, b; Pickersgill et al. 2021)

wave passage (solid-state deformation, that is, all that happens during shock metamorphism, including phase transformations) with subsequent thermal effects (diffusion; Nyquist et al. 1987). This can alter boundary conditions of isotopic equilibration and decrease the time required to reset ages in certain phases that have low diffusion rates (Nyquist et al. 1987). Therefore, it is important to assess the sample's origin, post-crystallization, and post-depositional history for context because geochronology interpretations depend on an understanding of the radiometric part equilibrating prior to parent/daughter fractionation as well as perturbation after achieving closure.

Impact effects on isotopic systems can be manifested by mineral age resetting or partial resetting, which is, in turn, dependent on conditions during and after impact (e.g., pressure, temperature, diffusion), and this may complicate age interpretations (in any systems; McDougall and Harrison 1999; Jourdan 2012; Tohver et al. 2012). For example, Jaret et al (2018b) compared $^{40}Ar/^{39}Ar$ ages of shocked diaplectic glass, impact melt, and target rocks at the Manicouagan impact structure, Canada. They found that diaplectic glass, produced as a response to shock compression, was partially reset, yielding ages indicative of neither the target nor impact age. Additionally, Jaret et al. (2018a) inferred Ar resetting in crystalline feldspar grains adjacent to and in contact with the melt sheet, possibly controlled by thermal effects from the impact. Partial resetting has been observed in the K–Ar system and $^{40}Ar/^{39}Ar$ method (Cassata et al. 2010; Weirich et al. 2012; Walton et al. 2014) in extraterrestrial lunar and meteoritic samples due to shock compression and heating and resulting loss of radiogenic Ar, as well.

Aside from geochronology, additional science investigations may favor returned samples that have experienced minimal shock. One such science objective has been outlined by recent reports from the Mars Exploration Program: reconstructing the processes that affected the evolution of the Martian dynamo by understanding the thermal and magnetic history of Mars (Beaty et al. 2019). Paleomagnetic measurements, if combined with geochronology measurements on a suite of returned samples, could improve our understanding of the Martian dynamo and its connection to climatic and planetary thermal and interior evolution (Mittelholz et al. 2018 and references therein; Beaty et al. 2019). Paleomagnetism studies may also benefit astrobiology analyses by constraining the potential preservation state of potential biosignatures in samples or by constraining the role of atmospheric erosion in Mars' habitability (Mittelholz et al. 2018; Beaty et al. 2019). Even though the effect of specific shock metamorphic features on the magnetic properties of rocks are not well constrained (e.g., Reznik et al. 2016), returned samples having experienced shock metamorphism are not recommended for paleomagnetic studies. Shock may cause complicating effects such as demagnetization of a rock (e.g., Rochette et al. 2003), secondary magnetization effects (e.g., Halls 1979), or modifications of magnetic anomalies (e.g., Hood et al. 2003).

Additionally, shock effects may reduce or alter the preservation of organic carbon or microtextures within rock, which would hinder biosignature analyses. At high pressures and temperatures associated with shock, organic matter could transform in many ways, including volatilization of S and other elemental groups, loss of starting organic matter (Tingle et al. 1991), particularly aliphataic groups, selective release of H isotopes (Mimura et al 2007), or even transformation of graphitic carbon to diamond (e.g., El Goresy et al. 2001).

1.1.3 Analyses Possible with Shock-Altered Samples

For the above reasons, highly shocked samples (considered here to be greater than ~ 35 GPa) are likely to be a low caching priority for MSR. However, in other cases, shocked samples may be desirable for MSR. Shocked samples may be useful to understand the timing of impact events. For example, highly shocked feldspars are more likely to provide reliable ages for impact events than low and moderately shocked (~ 5–20 GPa) materials (Jourdan 2012; Jaret et al. 2018b). Additionally, impact-affected rocks would be useful to improve the understanding of the early bombardment of Mars in the context of the putative late heavy bombardment epoch (Bottke & Norman 2017). Also, weathering and impacts may contain geochronologic indicators to help constrain the time of aqueous and impact activity (e.g., Jourdan et al. 2011).

An additional rationale for collecting shocked samples might be to sample atmospheric gases that were trapped in the samples at the time of shock. Several of the Martian meteorites were found to have atmospheric gases and volatiles trapped inside of them (Bogard and Johnson 1983; Wiens et al. 1986; Karlsson et al. 1992). Wiens and Pepin (1988) indicated that noble gases and nitrogen were trapped without fractionation. Residence timescales of several gases in the Martian atmosphere are short with respect to the age of the planet (Jakosky et al. 2017 and references therein), so recovery and measurement of trapped gases may be the best way to understand Mars' climate and volatiles as they existed at the time of shock. This would provide a unique window into Mars' atmospheric composition when the planet was more habitable.

2 Shock Effects in Feldspars

A variety of Jezero Crater surface rock types and their weathering products may be useful for geochronology studies. Igneous rocks give constraints on crystallization age of melts that could represent rocks derived from magmatic or impact melts (Newsom et al. 2015; Cohen et al. 2019). This review will focus on plagioclase feldspar. This is because feldspar is a major component of most igneous rocks, a rock-forming mineral in Martian crustal rock, and an abundant component of crystalline phases found on Mars' surface (e.g., in Gale crater sediments, as identified by the CheMin instrument onboard Mars Science Laboratory (Bish et al. 2013; Morrison et al. 2018; Rampe et al. 2020).

Feldspars show a range of complex deformation products after impact (Fig. 1; French 1968, 1998; Kieffer et al 1976; Ostertag 1983; Langenhorst 2002; Ferrière and Osinski 2013; Jaret et al. 2014, 2015, 2018a, b; Pickersgill et al. 2015, 2021). Shock effects in feldspars include crystallographic controlled fracturing, solid-state amorphization, phase transformation, and melting at high pressure (e.g., Ma et al. 2015). See Pickersgill et al. (2021) for a review.

A major shock effect visible in feldspar is the formation of amorphous feldspar-composition material, maskelynite. Because formation of amorphous material is achievable by different physical processes, some of which can occur together and over small spatial scales, this has resulted in inconsistencies in the literature over maskelynite's formation. Tschermak (1872) originally identified maskelynite impact melt glass, seen as an amorphous phase in the Shergotty meteorite of plagioclase, which retained grain boundaries and petrographic textures. Others concluded that maskelynite results from solid-state

amorphization processes (Bunch et al. 1967; Arndt et al. 1982; Jaret et al. 2015). How-ever, others still consider maskelynite a dense impact melt quenched at high shock pressure (Chen and El Goresy 2000). For this manuscript, we follow Pickersgill et al. (2021) and avoid using the term maskelynite to reduce confusion. We use the terms "diaplectic feld-spar glass" to indicate solid-state amorphous plagioclase and "melt glass" to indicate when there has been clear evidence of temperature increase-induced melting. "Glass" will be used to indicate an unknown formation mechanism or features occurring in both diaplectic and melt glasses. These distinctions affect geochronology interpretations since melting and quenching of a fused glass would produce a new material whose age would reflect the time close to the impact (the age when the melt cooled down to closure temperature), whereas a solid-state mechanism may not enable open-system behavior that would reset the K–Ar isotope age.

Shock effects in plagioclase occur as degradation of the crystalline order with increasing shock pressure (Stoffler 1971; Ostertag 1983; Heymann and Hörz 1990; Fritz et al. 2005). Feldspar disordering generally begins at pressures > 15–20 GPa, diaplectic feldspar glass formation occurs between ~ 25 and 45 GPa, and significant melting occurs above ~ 45 GPa (Bunch et al. 1967; Ostertag 1983; Heymann and Hörz 1990; Johnson et al. 2003; Johnson and Hörz 2003). However, precise melting ranges can be dependent on strain rate, initial temperature, water content, and shock pulse duration (Sims et al. 2019). The shock pres-sures at which structural disorder and melting occur depend on pre-shock rock properties, such as grain size, porosity, and composition (Ostertag 1983; Jaret et al. 2018a, b; Pick-ersgill et al. 2021).

3 Perseverance Rover Instrumentation for Shock Analyses

Although analyzing Martian meteorites is one of the best ways to understand natural shock processes on Mars, many challenges prevent the extrapolation of such information to the planet as a whole. Studies of shock metamorphic effects in meteorites generally involve assumptions about their parent lithology and formation regions, which may introduce inaccuracies when extrapolating shock levels from individual rocks to planetary surfaces (Sharp and DeCarli 2006; Kayama et al. 2012). Furthermore, Martian meteorites are rare in scientific collections, and the majority are young (less than 1 Ga), single-lithology igne-ous rocks, which do not represent the full diversity of Martian lithologies (e.g., Walton et al. 2008). Therefore, characterization of shock phases using the in situ instrumentation aboard Perseverance will be crucial in correlating the lithologies in Jezero crater to the samples that will be returned.

Because diaplectic glass-bearing rocks are not distinctive in hand samples or outcrop textures, the ability to distinguish these via in situ analyses could be critical for optimizing sample selection on Mars for geochronology studies. *Perseverance* includes seven payload instruments. Among them, two instruments house a combination of Raman and visible/ near-infrared spectroscopy techniques: SuperCam and Scanning Habitable Environments with Raman & Luminescence for Organics & Chemicals (SHERLOC).

SuperCam can obtain multiple types of vibrational, structural, mineralogical, and chem-ical information about organics, minerals, and elements (Maurice et al. 2021; Wiens et al. 2021). It is capable of characterizing mineralogy and composition, formation and altera-tion processes, and interpretations of geological context of the samples. SuperCam includes time-resolved Raman (532 nm ns-pulsed laser to remove daylight and luminescence from

Raman spectra), time-resolved luminescence (excited at 532 nm and analyzed in the range 535–850 nm), and visible-infrared (VISIR) spectroscopy. The spectral ranges are 150–4400 cm^{-1} (Raman), 536–850 nm (luminescence), and ~400–853 nm/1300–2600 nm (passive reflectance across three spectrometers). The spot size of the Raman/VIS and IR analyses varies with distance: 0.75 mrad (FOV) and 1.15 mrad, respectively (Maurice et al. 2021; Wiens et al. 2021), e.g. 2.25 mm and 3.45 mm in diameter at 3 m distance, respectively. SuperCam uses time resolution (to 100 ns) to potentially distinguish organic from inorganic fluorescence. Fluorescence originating from inorganic sources, with typical lifetimes > 1 μs, can be separated from organic fluorescence sources, which typically have lifetimes ≤ 100 ns (Bozlee et al. 2005; Misra et al. 2016; Beyssac 2020; Pasteris and Beyssac 2020).

Additionally, SuperCam's color remote micro-imager (RMI) provides context for targeted samples and characterize sample textures. Laser-induced breakdown spectroscopy (LIBS) provides compositions of major, minor, and trace elements. Finally, SuperCam includes a microphone to record the resulting LIBS plasma shock waves and to characterize rock hardness.

SHERLOC, an arm-mounted instrument, is intended to detect, characterize, and map organics and minerals in target rocks on the Martian surface (Bhartia et al. 2020). SHERLOC is a Deep UV (DUV) resonance Raman and fluorescence spectrometer utilizing a 248.6-nm DUV laser and ~100 μm spot size (Bhartia et al. 2020). SHERLOC's Raman spectral range is 800 to > 3600 cm^{-1} and its fluorescence spectral window is 274–354 nm (Bhartia et al. 2020). Note that certain minerals, such as silicates, such as orthoclase and microcline, may be identifiable down to ~470 cm^{-1}, depending on the strength of the Raman scattering (Razzell Hollis et al. 2021a). SHERLOC also employs two imagers, Wide Angle Topographic Sensor for Operations and Engineering (WATSON) and an autofocus and context imager (ACI), to provide contextual microimages and maps of targets and their surroundings.

SHERLOC is intended to help prioritize samples containing potential biosignatures for cache and MSR. The UV excitation wavelength chosen for SHERLOC is based on electronic resonances with various organic compounds, making it optimized for organic identification (Beegle et al. 2015; Bhartia et al. 2020). Additionally, it utilizes native fluorescence, a complimentary detection mode to Raman, which can distinguish organic from mineral sources with high sensitivity using the DUV excitation wavelength. The combined usage of these spectroscopy techniques on SHERLOC is designed to enhance the confidence of potential biosignature identifications (Bhartia et al. 2012; Shkolyar et al. 2018).

4 Spectral Features of Shocked Feldspars

This section reviews spectral features of the transition from crystalline plagioclase to glass with increasing pressure, as revealed in IR, Raman, and luminescence spectra. However, this is not an exhaustive review of the types of features that could be encountered with Mars 2020. Other shock-related minerals also detectable with these techniques on Mars include high-pressure quartz phases, ringwoodite, and phosphates (e.g., Ostroumov et al. 2002; Ohtani et al. 2006; Baziotis et al. 2013; Ma et al. 2015). For example, there is growing recognition that phosphates, such as monazite, (La,Ce,Th)PO$_4$, may be useful for recording shock ages (e.g., Deutsch et al. 1990; Schärer & Deutsch 1990; Tohver et al. 2012; Erickson et al. 2017; Kenny et al. 2020). Additionally, apatites (and zircons), key minerals for obtaining robust ages, may have stronger Raman and luminescence signatures than feldspars.

This could make them easier to identify with spectroscopy techniques. However, they are expected to be rare at Jezero crater and their REE-induced luminescence peaks (e.g., Sm or Nd) do not show systematic behavior with shock pressure changes (e.g., Gucsik et al. 2002).

4.1 Raman Spectroscopy

Raman spectroscopy is a vibrational spectroscopy technique based on inelastic scattering of light by a sample and is widely used to characterize shocked minerals. Raman is sensitive to low-frequency lattice modes and crystallinity in mineral crystals, making it ideal to characterize shock in feldspars (Velde et al. 1989; Fritz et al. 2005; Jaret et al. 2014; 2015).

The three most intense peaks for assessing shock level in plagioclase feldspars (An35-75) occur at ~509 cm^{-1}, ~485 cm^{-1}, and ~1030 cm^{-1}, based on studies of both natural and experimentally shocked samples. However, their exact positions vary with composition due to the solid solution within the plagioclase series (Mernagh 1991; Freeman et al. 2008; Befus et al. 2018). Plagioclase compositions in Gale crater have been found to be andesine compositions (An28–An43), based on in situ data from the CheMin instrument on Mars Science Laboratory rover (Rampe et al. 2020), while those of most Martian meteorites span a larger range, from andesine to labradorite (~An20–An70; Harvey et al. 1993; Fritz et al. 2005; McSween and Treiman 2018). The range of Raman active vibrational shift ranges for crystalline plagioclase is detailed in Table 1.

Feldspars end members each have their own slightly different Raman spectrum. However, individual modes related to all feldspars can be classified into groups that are related to frequency range, intensity, and vibration environment (e.g., Freeman et al. 2008). To systematize the complexity of the Raman response of different feldspar minerals, the sequential ν_1 to ν_{39} band frequency proposed by Aliatis et al. (2015) has been adopted in this work. Table 1 summarizes the mode assignments and their wavenumber range common for plagioclase feldspar minerals.

The exact peak positions vary with composition due to the solid solution within the plagioclase series (Mernagh 1991; Freeman et al. 2008). Table 2 summarizes the

Table 1 Raman mode assignments for crystalline plagioclase, where T = Si or Al

Classification of modes	Modes	Raman shift range (cm^{-1})	Mode assignment
Group III	$\nu_1–\nu_{10}$	< 200	Rotation-translation of SiO$_4$ tetrahedra and external bending of alkali cations
Group II	$\nu_{11}–\nu_{20}$	200–450	Rotation-translation of SiO$_4$ tetrahedra and external bending of alkali cations
Group I	$\nu_{21}–\nu_{25}$	450–580	Four membered rings of T–O–T stretching, bending and breathing modes. The most intense mode is ν_{24}
Group IV	$\nu_{26}–\nu_{31}$	600–800	Internal Si–O tetrahedra deformation. Affected by alkali cation content
Group V	$\nu_{32}–\nu_{39}$	900–1200	T–O stretch vibrations and breathing

Mode assignments are from Sharma et al. (1983), Mernagh (1991), Huang et al. (2000), McKeown (2005), Freeman et al. (2008), Aliatis et al. (2015), Jaret et al. (2015), and Befus et al. (2018)

Note that for less enriched anorthite plagioclases, the bands above 600 cm^{-1} are less intense and broader due to the influence of alkaline elements

Table 2 Proposed Raman bands for crystalline plagioclase minerals at room pressure and temperature, averaging the values proposed by Sharma et al. (1983), Mernagh (1991), Huang et al. (2000), McKeown (2005), Freeman et al. (2008), Aliatis et al. (2015), Jaret et al. (2015), and Befus et al. (2018)

Mineral	%Orthoclase	%Albite	%Anorthite		ν_{10}	ν_{14}	ν_{21}	ν_{22}	ν_{24}	ν_{25}	ν_{26}	ν_{29}	ν_{31}	ν_{32}	ν_{33}
Oligoclase	1.0–7.0	65.0–87.0	11.0–28.0	Mean	161.0	286.3	454.7	479.0	508.5	576.0	646.0	763.0	814.0		
				Sigma	1.0	3.2	0.7	0.9	1.9	1.3	1.4	3.1	1.2		
Andesine	0.0–6.0	49.0–56.0	36.0–50.0	Mean	176.2	286.3	447.6	480.7	510.0	571.0		767.0	797.0		
				Sigma	1.2	0.6	1.8	0.5	0.5	1.7		2.8	1.3		
Labradorite	1.0–3.0	36.0–46.0	51.0–62.0	Mean	180.0	285.9	446.0	480.5	509.0	567.0			792.0		984.0
				Sigma	2.1	0.3	3.5	0.7	0.2	1.6			0.9		2.6
Bytownite	0.0–1.0	20.0–24.0	75.0–80.0	Mean	196.6	285.4	460.6	484.4	504.6	561.0	682.0	765.0		913.0	980.0
				Sigma	1.8	1.6	1.8	1.3	0.5	1.5	1.3	3.2		1.1	2.2
Anorthite	0.0–1.0	1.5–3.0	96.0–98.0	Mean	193.9	283.9	439.0	486.9	504.7	558.0	672.5	766.5		913.5	980.0
				Sigma	2.5	1.6	20.0	1.1	0.9	1.4	1.6	3.5		0.7	4.2

proposed Raman peak values of the different plagioclase minerals obtained as the mean and standard deviation of reported bands at room temperature and pressure, valid for the range of anorthite/albite indicated for each solid solution. As seen, there are important differences in the wavenumbers of the different Raman bands to differentiate among oligoclase, andesine, labradorite, bytownite, and anorthite. The values proposed in Table 2 could be considered as the reference values for non-shocked plagioclase feldspars.

Upon increased shock pressure, Raman spectral observations of albite, andesine, and bytownite have revealed (1) decreased intensities or loss of most lattice mode bands, (2) significant broadening of the 900–1060 cm^{-1} (ν_{32}–ν_{39}) and 200–450 cm^{-1} (ν_{11}–ν_{20}) features, (3) convergence of ~475–487 cm^{1} (ν_{22}–ν_{25}) and ~505–510 cm^{-1} (ν_{24}) Raman bands at moderate to high pressures, and (4) shifts to higher wavenumbers (Velde et al. 1989; Fritz et al. 2005; Freeman et al. 2008; Befus et al. 2018; Jaret et al. 2018a; Johnson et al. 2020; Xie et al. 2020). For example, in albite, the 475 cm^{-1} peak merges with the ~505 cm^{-1} band at pressures above 8 GPa during hydrostatic compression in a diamond-anvil cell (Aliatis et al. 2017) while for albite and bytownite both bands are still clearly differentiated at pressures lower than 4 GPa (Befus et al. 2018; Torre-Fdez et al. 2018). Increasing shock pressures can shift bands between 475 and 600 cm^{-1} to higher wavenumbers in oligoclase, labradorite, andesine, and anorthite due to compression of the crystal lattice, as well (Velde et al. 1989; Befus et al. 2018). With increasing amorphization, similar trends are visible as with increased shock in feldspars. Examples can be seen in Fig. 2.
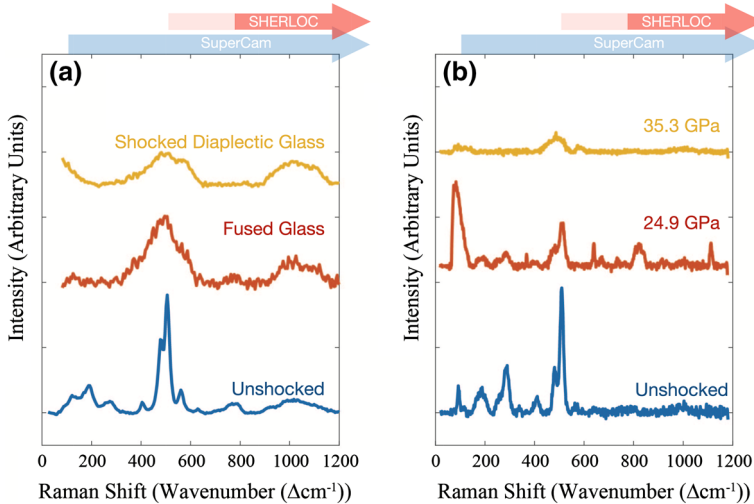

Fig. 2 Raman spectra of natural and experimentally amorphized feldspars. Natural diaplectic glass and unshocked labradorite (An$_{64}$) are from ejecta blocks at the Lonar Crater, India, our only example of a natural impact into Mars-like basaltic target material (Jaret et al. 2015). **a** Comparison of crystalline (blue), shocked (yellow) and fused (blue) labradorite from Jaret et al. (2015). Shock pressures for diaplectic glass were ~25–28 GPa. **b** Crystalline and experimentally shocked andesine from Jaret et al. (2018a, b), revealing decreased peak intensities with increasing shock. Peak shock pressures are indicated (in GPa). SHERLOC and SuperCam spectral ranges are noted in red and blue arrows. Lighter red shading on SHERLOC's spectral range indicates a limited ability to detect certain minerals at lower than 800 cm^{-1} (Razzell Hollis et al. 2021a). It should be noted that these are microscopic Raman spectra and comparison to rover instruments is cautioned

Diaplectic glass can be easily discerned from crystalline (or unshocked) plagioclase in a Raman spectrum. The two plagioclase-diagnostic peaks of crystalline plagioclase merge into a broad hump centered at ~ 570 cm^{-1} and a shoulder at ~ 580 cm^{-1} in a diaplectic glass spectrum (see Fig. 2). A peak is also often visible at 1000–1200 cm^{-1} in glass but absent in crystalline plagioclase due to the lack of non-bridging O atoms in well-crystallized tectosilicate (Fritz et al. 2019; Xie et al. 2020; Fig. 2–3). The diaplectic glass spectrum is clearly contrasted from the crystalline and unshocked plagioclase (Fig. 2, both bottom spectra), showing a sharp double band at 475–510 cm^{-1} and another at 580 cm^{-1}, due to an increase in the number of three-membered rings of tetrahedra (Fritz et al. 2019). Some Raman bands may vary with intensity in diaplectic glass, due to the localized short-range order of the inhomogeneous nature of diaplectic glass, or due to the increased numbers of non-bridging Si–O and Al–O after shock pressure/temperature changes (Xie et al. 2020).

Raman band parameters, in the absence of additional compositional data, are unreliable indicators of shock extent. For Raman peak ratios and band positions, no systematic, reliable trends are revealed with pressure changes (Fritz et al. 2005; Baziotis et al. 2013; Jaret et al. 2018a). For instance, spectral differences of progressively shocked feldspars can mimic those of unshocked feldspars of varying compositions. Raman peaks shift with solid solutions because they affect the lattice environment by shifting bond angles, lengths, and strengths (Befus et al. 2018). For example, the 575 cm^{-1} and 515 cm^{-1} Raman bands can shift linearly with varying Na composition in plagioclase and alkali feldspars (Freeman et al. 2008; Befus et al. 2018). Raman bands between 385–447 cm^{-1} and 856–897 cm^{-1} can shift with variable Fe composition in orthopyroxenes since the Na cation translates along the X-axis (Huang et al. 2000; McKeown 2005). Bands between 475 and 600 cm^{-1} could be mistaken for various types of feldspars of similar compositions that have been shocked to 0.1–10 MPa (Sect. 2.2; Geiger and Kolesov 2002; Befus et al. 2018). Additionally, the influence of Na/Ca and Si/Al ratios on peak position and intensity is poorly constrained in Raman spectra (Xie et al. 2020). K-feldspar exsolution can be discerned from plagioclase by their Raman features to some extent, but according to Xie et al. (2020), Raman peak positions are usually insufficient for obtaining compositional information on plagioclase solid solutions.

Approaches which do not rely on single band parameters have been explored to correlate shock pressure with spectral information, including assessments of peak ratios and standard deviations. In diaplectic feldspar glass, the 485/509 cm^{-1} ratio decreases with high enough shock pressure (> 45 GPa), splitting into two bands at 490 and 505 cm^{-1}, due to plagioclase recrystallization (Fritz et al. 2005). Up to 50 GPa, the 479/507 cm^{-1}

Fig. 3 Micro-Raman spectrum of diaplectic glass (labradorite, An64) from a shocked basalt obtained in Lonar Crater, India
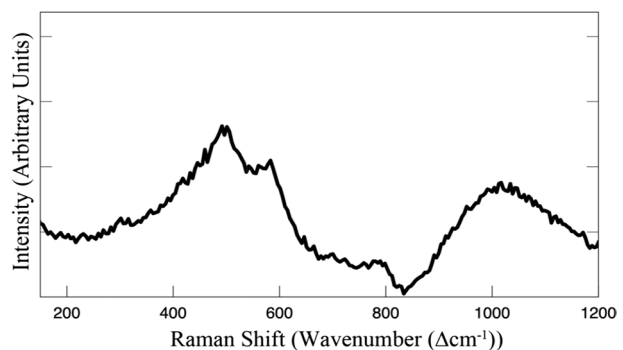
peak ratio may approach 1 and/or the 485/509 peak ratio can decrease in albite (Jaret et al. 2018a). Standard deviations of spectral band positions and intensities at increasing pressures have been used to gauge how accurately certain techniques can be quantitative indicators of shock (Kayama et al. 2012; Jaret et al. 2018a; Johnson et al. 2020). This is because at low shock pressures, there are individual energy barriers/heterogeneities that give local variability, while at higher shock, higher energy causes less heterogeneity to be evident. Additionally, a progressive decrease in the standard deviations of Raman the band intensities can be observed with increased shock pressure in albite, andesine, and bytownite (Jaret et al. 2018a).

Rather than attempting to extrapolate single pressure values from Raman spectra, Fritz et al (2005) defined four ranges of equilibrium shock pressure estimates: (1) pressures below 26 GPa and diaplectic plagioclase versus unshocked plagioclase, indicated by differences in FWHM of characteristic Raman bands and reduced band intensities as compared to the luminescence background; (2) spectra characteristic of maskelynite and bands at 505 cm^{-1} and 590 cm^{-1}, indicating pressure ranges between 26 and 40 GPa; (3) maskelynite at pressures from 40 to 45 GPa and a relaxation in the diaplectic glass structure, indicated by a low-intensity 590 cm^{-1} band; and (4) shock pressures over 45 GPa and recrystallization of plagioclase, indicated by splitting of the 505 cm^{-1} band into bands at 490 cm^{-1} and 505 cm^{-1}. However, it should be noted that these ranges were estimated from Martian meteorites, and it is unclear how accurate the calculated shock pressures of the associated Martian impacts are.

Background luminescence, when captured in a Raman spectrum, appears as a broad hump and can also increase with increased shock pressure (Heymann and Hörz 1990; Fritz et al. 2005; Pittarello et al. 2020). While luminescence is commonly seen as an impedance in the weaker Raman spectrum because of this background, it often carries useful information about the target sample when a dedicated luminescence spectrum is collected separately (see following section).

4.2 Luminescence Spectroscopy

Luminescence is used here to describe all photoluminescence phenomena (e.g., fluorescence, luminescence, or phosphorescence; Beyssac 2020). Photoluminescence allows discrete energy levels of a sample to be excited, which makes it possible to distinguish among various luminescence centers (Nasdala et al. 2004).

One common form of luminescence spectroscopy is cathodoluminescence (CL), which measures the emission of photons from a material stimulated by an electron beam (e.g., Götze et al. 2000). Limited work has been done on CL properties of progressive shock metamorphism and amorphization of plagioclase and glass. A variety of luminescence features can be seen in feldspars due to lattice defect centers or cation substitutions with increasing shock pressure (e.g., Götze et al. 2000; Kayama et al. 2012, 2018).

It is reasonable to assume that CL analyses may be used as a tool to guide interpretations of luminescence spectra of shocked minerals on *Perseverance* Rover. However, direct comparisons between laboratory CL data and SuperCam and SHERLOC luminescence data have limited applicability. This is primarily because emission features are dependent on the excitation source. CL studies stimulate samples with a high-energy electron beam, while SuperCam and SHERLOC involve laser-induced (optical) luminescence (fluorescence). Because of this difference, CL lab studies should not be considered as reliable

analogs of data sets obtained by SuperCam and SHERLOC's laser-induced fluorescence spectroscopy capabilities.

A related technique, optically stimulated luminescence (OSL), may have some applicability to identifying shock extent in samples on Mars using SHERLOC (Cohen et al. 2019). OSL has been investigated as a shock indicator (Smith et al. 1986; Godfrey-Smith et al. 1988; Spooner 1994; Nasdala et al. 2004) and as a Mars analog sample dating technique (Jain et al. 2006). OSL is based on trapped charge released as luminescence upon photon irradiation, coming from the decay of naturally occurring radionuclides and cosmic rays. See Nasdala et al. (2004) for a review. OSL is sensitive to thermal conditions imparted by even mild shock events, erasing the emission signature in seconds by heating to 200–400◦C. OSL can potentially be useful for geochronology by determining the duration of daylight exposure for rock surfaces, which can complement surface exposure dating techniques using cosmogenic nuclides. This analysis may indicate a sample's shock history by determining whether it has been heated above a threshold temperature. The technique has been successfully used to date quartz and feldspar in terrestrial sedimentary and volcanic samples at a variety of wavelengths (Smith et al. 1986; Godfrey-Smith et al. 1988; Spooner 1994), though not yet in the range relevant to SHERLOC, the deep UV. On *Perseverance*, OSL may possibly be measurable with SHERLOC and the WATSON CCD, since feldspar emits in the range detectable by it (500–600 nm; Bailey et al. 2011). However, this technique poses several challenges. It is unlikely to unlikely to provide quantitative exposure dates without extensive calibration and assumptions about the geologic history of the sample and the Martian surface cosmic ray flux, which is a crucial aspect for interpreting the meaning of the luminescence signal. Additionally, the rover's instruments were not designed or tested for this technique. Additional work is needed to determine the extent to which OSL can guide the identification of shocked samples for caching and MSR.

4.3 IR Spectroscopy

In addition to Raman spectroscopy, there have been many studies of the effects of shock on feldspars using IR spectroscopy. IR spectroscopy is a useful tool for mineral identification because it probes specific vibrational modes of mineral crystal lattices. IR spectroscopy is generally divided into the mid-IR (MIR), also called the thermal IR, from ~5 to 50 μm (~2000–200 cm^{-1}), and the visible to near-infrared (VNIR), from 0.3 to 5 μm.

Most IR spectroscopy shock studies have focused on the thermal IR region (~6 to >25 μm) for planetary science applications, such as interpreting data from orbiting spacecraft, Earth-based telescopes, and in situ observations of feldspar-rich surfaces on the Moon, Mercury, and asteroids (Johnson et al. 2002, 2003; Johnson and Hörz 2003; Reitze et al. 2021). For studies of shocked planetary analog materials, the focus on spectroscopic studies has also been mainly in the MIR since that wavelength range is useful to detect silicate minerals with characteristic absorption and reflectance bands due to vibrations of the Si and O framework (Pieters and Englert 1993; Johnson et al. 2002, 2003a; Johnson and Hörz 2003; Johnson 2012; Jaret et al. 2015, 2018a, b). Few laboratory studies have been performed in the VNIR on experimentally (Johnson and Hörz 2003) or naturally (Pieters 1996) shocked feldspars. An added challenge of VNIR for shock identification is that VNIR band positions depend on specific feldspar composition, local chemical environment, degree of Si-Al order, grain size, and/or substitutions. Finally, the use of MIR and VNIR spectroscopy on mission payloads is limited. Both the Spirit and Opportunity Rovers included a MIR instrument (Mini-TES). SuperCam employs the visible and lower

portion of the NIR range (0.4–2.6 μm), in which range shock effects in feldspars are significantly less explored and reveal ambiguous trends, as described below.

Shock-altered spectral changes discernible in IR spectroscopy are known in one important Mars-relevant mineral group: phyllosilicates. If clay-bearing Martian samples are returned to Earth, they would be valuable as geochronologic tracers of aqueous alteration (Hamilton et al. 1992; Swindle et al. 2000), which improve interpretations of diagenetic processes on ancient Mars. For example, obtaining the absolute ages of clay-bearing samples and their relationships with other processes (e.g., fluvial activity) could constrain the timing of aqueous conditions within Jezero crater (Cohen et al. 2019).

In clays, impact-altered features occur from deformation of the Si–O fundamental bending and stretching vibrations of the tetrahedral sheet, seen in the MIR, and from octahedral sheet vibrations, seen in the VNIR (Gavin et al. 2011; Michalski et al. 2017; Friedlander et al. 2015). Illustrations of these features for nontronite are provided in Fig. 4 at NIR and MIR wavelengths. Impact-induced structural disorder in the octahedral and tetrahedral sheets of smectites produces noticeable spectral changes in the MIR and the VNIR in the
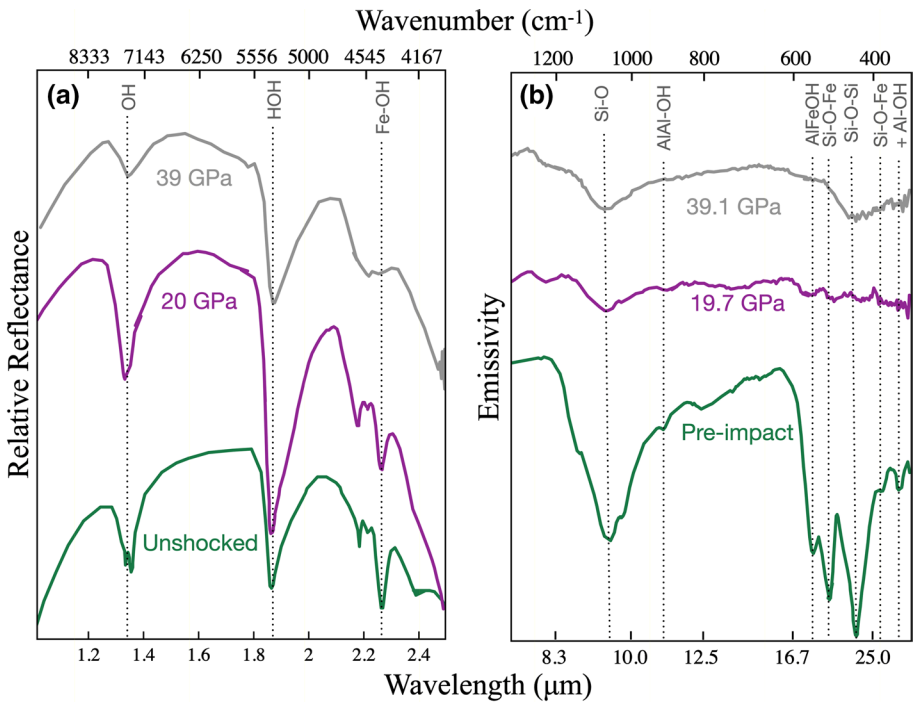

Fig. 4 Examples of IR spectral changes in nontronite with increasing shock pressure, between ~ 20 and 40 GPa, after undergoing experimental shock, at **a** NIR and **b** MIR ranges. **a** NIR reflectance spectra of nontronite are shown at the pressures indicated in GPa (Michalski et al. 2017). OH corresponds to hydroxyl deformation overtones located near 1.4 μm, HOH corresponds to vibrational overtones in adsorbed H_2O, and Fe-OH features for nontronite are located at ~ 2.28–2.29 μm (Michalski et al. 2017). **b** MIR emissivity spectra of nontronite are shown at the pressures indicated in GPa (Friedlander et al. 2015). The Si–O–Si bending mode, and Si–O stretch band, Al–OH bending mode, Al–OH deformation, and Si–O–Fe bending mode are indicated (Friedlander et al. 2015). Increasing impact pressure in nontronite causes reduction or loss of all Al and Fe bands, and only those resembling amorphous, hydrated silica (Si–O and Si–O–Si bands) remain in the MIR at ~ 39 GPa. Spectra have been offset (vertically) for clarity

range of 10–40 GPa (Friedlander, et al. 2015; Fig. 4). For example, upon increasing pressure (20–40 GPa) structural disorder causes spectral features to appear in nontronite similar to those of hydrated amorphous silica in the MIR or those of allophane-like phases in the VNIR (Friedlander et al. 2015). See Fig. 4 for an example. Smectite absorption features centered at 2.2 and 2.29 μm reduce in FWHM at shock pressures of > 25 GPa, indicating the formation of secondary amorphous phases (Friedlander et al. 2015). Other features disappear between 19 and 25 GPa and merge at > 34 GPa, indicating that structural deformation in the octahedral sheet that begins at low pressures and is completely deformed at high pressures (Friedlander, et al. 2015). The onset of deformation in the octahedral sheet occurs at ~ 10 GPa and total deformation is observed by > 30 GPa (Friedlander et al. 2015).

Despite these useful studies, MIR and VNIR spectroscopy by itself is generally insufficient to make the distinction between shock and other geological processes in clays. Impact-altered smectites have similar features as hydrated aluminum-rich amorphous silicates in VNIR spectra (Friedlander et al. 2015; Fig. 4). Additionally, in most cases, shock effects do not dominate NIR spectra for pressures between 10 and 40 GPa in clays (Friedlander et al. 2015; Michalski et al. 2017) or in carbonates (but slight changes in secondary absorption features have been observed; Pan et al. 2018).

5 Challenges, Recommendations, and Further Work

Based on literature on shocked plagioclase feldspars studies in the lab, potential challenges for analyses of shocked minerals using SuperCam and SHERLOC may occur on Mars. These challenges include the scale at which shock effects occur (Sect. 5.1) and the non-uniqueness of spectral bands as shock indicators (Sect. 5.2). Recommendations are offered for these challenges for both lab-based shock studies and in situ analyses with *Perseverance*. Other considerations, including those for analyses not relying on single spectral band parameters for more confident shock identifications (Sect. 5.3) and potential challenges of temperature-induced spectral shifts mimicking shock effects (Sect. 5.4) are also explored in the following section.

We acknowledge that there are often significant differences between material properties and instrument capabilities of small-scale, high resolution lab measurements versus bulk, coarser resolution remote measurements (Bishop et al. 2019). For example, grain roughness, incidence angle, and spot size differences can lead to complications for remote interpretations. Specifically, when looking at shock effects, grain orientations can be critical for single-grain lab analyses, whereas remote measurements are often bulk analyses that provide average orientations (Jaret et al. 2018a, b). Although we recognize these challenges in comparing laboratory measurements with remote observations, they remain the only way to inform, improve, and ground-truth remote planetary surface measurements.

5.1 Micro-scale Measurement Considerations

The scale of shock deformation is a challenge for the spectral detection of shock effects, even in laboratory studies. For low to moderate shock levels (~ 25–35 GPa), the deformation occurs as atomic dislocations or planar deformation features. These features occur within crystalline grains on scales of ~ 1–100 microns, measurable using state-of-the-art Raman laboratory instruments with laser spot sizes on the order of a few μm (French 1968; Jaret et al. 2014, 2018a). Even if single grains are successfully located, increasing homogenization seen with increasing shock pressure may prevent precise shock pressure

calibrations at the grain scale with spectroscopy (Jaret et al. 2018a). Micro-scale heterogeneities in individual grains contain amorphous and crystalline materials, with more heterogeneity visible at lower shock regimes (Sharp and DeCarli 2006; Jaret et al. 2014, 2018a). Additionally, variations in features related to micro-scale shock effects in basaltic rocks could be a result of the mixing between shocked and unshocked materials in Raman (and in thermal IR) spectra (Johnson et al. 2020). Analyses on scales larger than the inhomogeneities of shock features (> 100 microns) may yield "averaged" structural information of the region sampled (Velde et al. 1989), a potentially advantageous effect to mitigate spectral shifts caused by crystal orientation, in Raman and IR spectroscopies (Jaret, et al. 2018a; Johnson et al. 2020; Xie et al 2020).

SuperCam's Raman field of view is on ~ mm scales (e.g., ~ 2.25 mm at 3 m distance; Wiens et al. 2021). Still, shock may be detectable with SuperCam spectroscopy analyses if single grains are able to be interrogated. It is recommended that single, coarse grains be targeted within SuperCam's laser sampling volume to increase the probability of identifying μm-scale shock effects using mm-size Raman observations.

Even if mm-sized regions of interest are identified in high-resolution images, the ability of the SuperCam instrument to target such regions is dictated by the pointing accuracy of the Remote Sensing Mast (RSM). Experience with MSL has shown that pointing accuracy is subject to uncertainties in the 3D location of a given target (as determined by topographic models derived from Navigation Camera stereo images), as well as uncertainties in the RSM mast motion (e.g., tilt of the rover influenced by robotic arm's position). Such effects may lead to pointing offsets on the order of the feature's size, but they are small and likely to be compensated as experience is gained with the rover system. In the first three months of the mission, the instrument was able to target features as small as 2 mm in size.

Micron-scale Raman measurements on shocked mineral grains may be obtainable with SHERLOC, which interrogates ≤ 100 μm scale features (Beegle et al. 2015). However, it is unclear whether SHERLOC can aid in shocked mineral investigations for two reasons. (1) SHERLOC analyses are more likely to prioritize organic investigations over mineral analyses and (2) its Raman spectral range (Sect. 3) begins above most features associated with many mineral bands. Detections of feldspar Al–O or Si–O stretching vibrations at 900–1200 cm^{-1} (Table 1) may be the most likely shock detections with SHERLOC, although its spectral cut-off may extend below the stated range of 800 cm^{-1} in certain strong mineral peaks (Sect. 4.1; Razzell Hollis et al. 2021a). Studies are ongoing by the authors to assess the extent to which a UV (266-nm) Raman and luminescence spectroscopy instrument (Shkolyar et al. 2018, 2021), operating with similar acquisition parameters to SHERLOC, will be able to detect and characterize experimentally shocked feldspar samples (those from Johnson et al. 2002). It would be useful for further work to explore shock identification with UV Raman and luminescence spectroscopy systems analogous to SHERLOC to understand the extent to which it can identify shock in minerals on Mars.

If SHERLOC is able to capture maskelynite features, its Raman spectrum is likely to be significantly weaker than surrounding crystalline phases captured in the laser's sampling volume (Wang et al. 2004a, b). A micro-mapping approach used by SHERLOC can mitigate this effect. This strategy involves a point-counting traverse, where the surface of a target is scanned at fixed distance intervals along a linear traverse and spectra are taken at selected intervals, with laser focused only at the first point (Wang et al. 2004a, b). This method allows a larger compositional area to be sampled, making it useful for unprepared rock surfaces encountered with a rover, even if it results in a reduced signal-to-noise ratio. The accuracy of this technique depends on the characteristics of the minerals sampled and the traverse settings but may yield identifications similar to those obtained with

petrographic point counting methods (Haskin et al.1997; Wang et al. 2004a). If attempting to identify maskelynite or diaplectic feldspar glass with SHERLOC, a micro-mapping point-counting traverse approach is recommended. It is important to identify grains large enough to fill the sampling volume of the laser such that the signal of maskelynite or glass is the main contributor to the spectrum.

One final recommendation to explore whether shock assessments can be made using SHERLOC involves luminescence spectroscopy. Since OSL has been used to successfully date feldspar samples at a variety of wavelengths, but not yet the DUV (Sect. 4.2), analog laboratory studies should assess whether DUV-excitation OSL can guide SHERLOC-based shock analyses.

Perhaps a useful way forward for shock studies on *Perseverance* may be through *combined* data sets from UV and visible laser-induced Raman (and/or luminescence) spectra, like those obtainable from SHERLOC and SuperCam. This is the case with multi-wavelength Raman studies looking at the structure of carbonaceous materials in the visible and UV, which can provide information about carbon structure inaccessible from single-wavelength Raman spectra. This is possible via plotted relationships between Raman spectral peak positions and laser excitation wavelengths (Ferrari and Robertson 2001; Ferrari et al. 2004). No known work has examined whether any structural information can be inferred from a similar multi-wavelength analysis in shocked minerals (although volumes interrogated would be different in the two cases and may affect results). Further work should examine whether multi-wavelength (combining UV and visible excitation) spectroscopies, Raman and/or luminescence, can assess shock level in Mars relevant samples better than single-wavelength spectroscopy.

5.2 Non-uniqueness of Spectral Bands as Shock Indicators

One significant challenge facing any spectral shock identifications on Mars may be that spectral peak identifications, *on their own*, are not unique or definitive indicators of specific shock level (Sects. 4.1 and 4.2). In the IR, shock effects may produce similar spectral shifts to those indicating changes to the Fe^{3+} bonding environment in metal–OH bands, varying Fe/Mg abundances, semi-amorphous phyllosilicates, hydrated amorphous silicates, and others (Poulet et al. 2005; Friedlander, et al. 2015). In Raman spectra, peaks shift with shock extent, but also with changes in solid solutions, and factors such as bond angles, lengths, and strengths within the same mineral family (Befus et al. 2018).

Spectral data used for any shock interpretations should be complemented with chemical data on the same samples. Onboard *Perseverance*, chemical data will be obtainable via abundances and distributions of a wide range of elements using SuperCam's LIBS capability, as well as with PIXL (Planetary Instrument for Xray Lithochemistry). PIXL, a robotic arm-mounted micro-X-ray fluorescence (XRF) spectrometer, will collect texturally correlated elemental chemistry in areas up to cm^2 with a spatial scales as small as 0.03 mm (Allwood et al. 2020). Although the diffraction peaks could interfere with the quantification of elemental peaks, their absence in multiple grains of similar chemistry indicates if a phase under the beam is either fine grained or truly amorphous. This could allow constraints on diaplectic glass versus quenching after shock melting. This may be enough to determine composition of an individual mineral grain only if it is the same size or larger than the beam size diameter of the respective instrument (~ 125 um for PIXL x-ray beam; ~ 350 um for SuperCam laser beam).

Although progress is being made towards increasing Raman and IR lab databases on shocked feldspars (e.g., Johnson and Hörz 2003; Johnson 2012; Jaret et al. 2015), there

is still a literature gap on spectroscopy studies of experimentally shocked feldspars over a wide range of shock levels, particularly in *naturally* shocked terrestrial impact structures (Xie et al. 2020). This suggests that further studies need to be performed on this topic to improve the confidence of *Perseverance*'s shock interpretations. The creation of lab databases using shocked and unshocked feldspars would be very helpful. These could correlate spectroscopic data (VNIR and/or Raman) with compositional (PIXL-like or LIBS-like) data to catalog differences in shock extent versus composition within closely related mineral types. These studies should clearly differentiate minerals of (a) different shock levels, as identified by different spectroscopies, (b) unshocked feldspars with compositional (especially Fe and Fe/Mg) differences, and (c) different solid solutions within one mineral series. Similar databases should also be developed for shock-altered clay- and carbonate-bearing phases and additional minerals relevant for geochronology (Sect. 4.3).

5.3 Shock Indicator Strategies Not Relying on Single Band Parameters

As illustrated here, attempting to infer discrete pressures from spectral data could be challenging for shock identification with *Perseverance*. Instead of using single spectral band parameters to indicate shock extent, one potentially more reliable approach for SuperCam or SHERLOC could include identifying pressure range categories, such as the Raman ranges described in Fritz et al. (2005) in Sect. 4.1. Even higher confidence shock interpretations are likely to result if discriminating between shocked and unshocked *endmembers*. For example, Raman can reliably discriminate between diaplectic glass and unshocked crystalline plagioclase (Xie et al 2020; Sect. 4.1). Figures 2–3 illustrate this, as well as that distinctions between crystalline vs. glassy feldspars are more clearly recognized in Raman spectra than are distinctions between shocked vs. fused (laboradorite) samples. SuperCam and SHERLOC Raman observations will be more likely to achieve a simple discrimination between glassy vs. crystalline feldspars when attempting to identify shock extent in feldspars than to infer discrete pressures or even pressure ranges from Raman spectral data.

However, even if maskelynite were present on Mars, its confident detection may be confounded by the presence of amorphous or glassy material with similar spectral properties. This is suggested by the significant proportion (~ 27 wt%) of material at the Rocknest site which was found to be XRD-amorphous, interpreted as primary glass and aqueously altered material like allophane or iron oxides (Bish et al. 2013). This is also because maskelynite, as seen in Martian meteorites, is likely produced by the shock event that launched them off the Martian surface (Rubin 2015), suggesting that shocked minerals in Martian ground lithologies may be comparatively rare. The geologic interpretation of a unit would also provide necessary context to understand whether shock is the most likely explanation for glassy and amorphous spectral features (cf., Johnson et al. 2020). The identification of X-ray amorphous materials combined with elemental chemistry from PIXL would further help determine if the glassy material is feldspathic, iron oxide-rich, or altered material.

Another approach that may be useful for improving the reliability of any spectral data to infer shock extent is to assess the uncertainties of spectral band peak positions and intensities with changing shock pressures. Examples are discussed in Sect. 4.1 for Raman spectroscopy. This has also been observed in albite and andesine thermal IR spectra, where, for example, increased shock was associated with a reduction of the standard deviation of the 1103 cm^{-1} reflectance band (Jaret et al. 2018a). Continued laboratory work examining similar standard deviations would be useful to understand the effectiveness of such *uncertainties* of positions and intensities of IR, Raman, and luminescence bands for quantifying

shock extent (caused by natural variations in the sample) as compared to spectral bands *alone*. This may lead to quantitative approaches for interpreting shock extent spectroscopically in the lab and on Mars.

5.4 Temperature-Induced Spectral Changes Mimicking Shock Effects

Raman and luminescence spectral features of feldspars have been scarcely studied at the range of surface temperatures expected at Jezero (~ 150–300 K; Pla-García et al. 2020). One concern is that very low temperatures could cause spectral shifts in SuperCam and SHERLOC spectra that mimic shock alteration. Such shifts have been seen in laser-induced luminescence spectra of alkali feldspars, where features shifted to longer wavelengths at low Mars temperatures (Bozlee et al. 2005). However, the Raman and luminescence spectral resolution of SuperCam (12 cm^{-1}) full-width at half maximum and SHERLOC (~ 40.3 cm^{-1}; Razzell Hollis et al. 2021b) is greater than shifts expected due to temperature fluctuations on the surface (between 150 and 300 K). These temperature-induced shifts are < 3 cm^{-1} for olivine (Weber et al. 2014) and potentially similar for other minerals. Based on this, temperature-induced spectral peak shifts are unlikely to affect spectroscopy analyses on *Perseverance*.

6 Summary and Conclusions

The ages of Martian geological events could be best understood once their stratigraphy is tied to an absolute chronology via dating of Martian rocks returned to Earth. The first step of returning samples to Earth is now in progress, at the time of this writing, as part of *Perseverance* rover's MSR campaign. Perseverance is now performing in situ characterizations and selections of samples for cache and return to Earth. Samples are being prioritized based on their ability to enhance the understanding of Mars' geochemical history and astrobiological potential.

This review has explored considerations surrounding the selection of samples for cache with *Perseverance's* spectroscopy instruments, SHERLOC and SuperCam, for geochronology analyses in terrestrial labs. We focused on one Mars-relevant mineral type, plagioclase feldspar, and impact-induced changes in its spectral signatures (with a brief review of impact-altered clay- and carbonate-bearing mineral signatures as well). Impact metamorphism of feldspar, and by extension, other minerals in the affected rock, can disturb isotopic systems and therefore weaken geochronology interpretations (as well as paleomagnetism studies and biosignature detection efforts). In other cases, shocked feldspar (and the larger sample of which it is part) may be desirable to cache for Earth return because they may be useful to constrain Mars' early bombardment history or its volatile evolution (via atmospheric gases trapped in a sample at the time of shock).

We have reviewed spectroscopic shock indicators revealed by SuperCam and SHERLOC, which will obtain Raman, luminescence, and VNIR spectra on Martian samples. We have focused on Raman spectroscopy studies. This is because Raman is the most well-developed of the three spectroscopies to inform shock studies on planetary surfaces and the most sensitive technique to identify feldspar structure onboard *Perseverance*. Luminescence lab studies have limited applicability to *Perseverance* instruments, and VNIR studies on shocked minerals have not yet yielded robust trends for feldspars.

Even though much has been learned from studies defining the ability of Raman spectroscopy to characterize shock extent in minerals, especially feldspars, Raman analyses on Mars are likely to encounter two major challenges. These include (1) the scale of laser beam sizes being large with respect to that of shock features and (2) spectral peak identifications being poor shock indicators, when considered without additional information. Based on these challenges, we have made eight recommendations to enhance the science return of shock investigations on Earth. Three of them refer to direct analyses on Mars, and five refer to supporting laboratory studies to inform *Perseverance's* in situ spectral interpretations of shock-induced deformation, as follows:

On Mars:

- Interrogate single, coarse grains (if available) with SuperCam's laser to increase the probability of identifying μm-scale shock effects using a mm-size Raman laser beam.
- If identifying maskelynite or diaplectic glass with SHERLOC, perform a micro-mapping point-counting traverse approach and identify grains large enough to fill the sampling volume of the laser (such that the signal of maskelynite is the main contributor to the spectrum).
- Target first-order endmember identifications (glassy versus crystalline phases) in feldspars rather than discrete pressures or pressure ranges to provide the most reliable shock discriminations.

In supporting lab studies:

- Explore shock identification with UV spectroscopy analyses analogous to SHERLOC to understand to what extent it can characterize shock extent.
- Assess the potential for Raman and luminescence multi-wavelength (UV and visible excitation) spectroscopies for shock identification.
- Assess the potential of OSL at DUV wavelength excitation to guide shock sample analyses using SHERLOC.
- Create lab databases using shocked and unshocked samples which correlate spectroscopic data (VNIR and/or Raman) with compositional data (PIXL-like or LIBS-like) to catalog differences in shock extent versus composition for feldspars and related mineral types, as well as clay-bearing, and carbonate-bearing phases.
- Assess the effectiveness of using the uncertainties (i.e., standard deviations) of spectral values of the characteristic Raman and IR bands for quantifying shock extent.

Finally, this work only investigated shock indicators in feldspars and, briefly, in clay-bearing minerals. Other minerals may or may not respond to impact in the same manner as feldspars, even though all minerals are expected to be affected by impact. To fully optimize the success of geochronology measurements on Earth in samples returned from Mars, an improved understanding of spectroscopic shock indicators is necessary in feldspars as well as in additional datable minerals to be encountered by *Perseverance*.

Author Contributions BAC initiated the idea for shock feature identification using the Perseverance payload. SS performed literature searches and drafted the work. SS, SJ, and SH-A created all figures. All authors provided substantial and critical revisions on previous versions of the manuscript. All authors read and approved the final manuscript.

Declarations

Conflict of interest The authors have no conflicts of interest to declare that are relevant to the content of this article.

References

I. Aliatis, E. Lambruschi, L. Mantovani, D. Bersani, D. Ando, D. Gatta, P. Gentile, P. Salvioli-Mariani, M. Prencipe, M. Tribaudino, J. Raman Spec. **46**, 501–508 (2015)

I. Aliatis, E. Lambruschi, L. Mantovani, D. Bersani, G.D. Gatta, M. Tribaudino, P.P. Lottici, Phys. Chem. Miner. **44**, 213–220 (2017)

A.C. Allwood, L.A. Wade, M.C. Foote, T. Elam, J.A. Hurowitz, S. Battel, D.E. Dawson, R.W. Denise, E.M. Ek, M.S. Gilbert, M.E. King, Sp. Sci. Rev. **216**, 1–132 (2020)

J. Arndt, W. Hummel, I. Gonzalez-Cabeza, Phys. Chem. Miner. **8**, 230 (1982)

R.M. Bailey, E.G. Yukihara, S.W.S. McKeever, Rad. Meas. **46**, 643–648 (2011)

I.P. Baziotis, Y. Liu, P.S. DeCarli, H.J. Melosh, H.Y. McSween, R.J. Bodnar, L.A. Taylor, Nat. Commun. **4**, 1–7 (2013)

D. Beaty, M.M. Grady, H.Y. McSween, E. Sefton-Nash, B.L. Carrier (and the iMOST Team), Meteorit. Planet. Sci. **54**, S3-S152 (2019)

L. Beegle, R. Bhartia, M. White, L. DeFlores, W. Abbey, Y.-H. Wu, B. Cameron, J. Moore, M. Fries, A. Burton, *2015 IEEE Aerospace Conference*, Big Sky (7–14 March 2015)

K. Befus, J.-F. Lin, M. Cisneros, S. Fu, Am. Miner. J. Earth Planet. Mater. **103**, 600–609 (2018)

O. Beyssac, Elements Int. Mag. Mineral. Geochem. Petrol. **2**, 117–122 (2020)

R. Bhartia, L.W. Beegle, L. De-Flores, W. Abbey, J.R. Hollis, K. Uckert, B. Monacelli, K.S. Edgett, M.R. Kennedy, M. Sylvia, D. Aldrich, Sp. Sci. Rev. **217**, 1–115 (2020)

R. Bhartia, W. Hug, R. Reid, *Proceedings SPIE* 8358 (2012)

D.L. Bish, D.F. Blake, D.T. Vaniman, S.J. Chipera, R.V. Morris, D.W. Ming, A.H. Treiman, P. Sarrazin, S.M. Morrison, R.T. Downs, C.N. Achilles, Science **341**, 6153 (2013)

J. Bishop, xxx, in *Remote Compositional Analysis: Techniques for Understanding Spectroscopy, Mineralogy, and Geochemistry of Planetary Surfaces*. ed. by J. Bishop, J. Bell III., J. Moersch (Cambridge Planetary Science, Cambridge, 2019), pp. 68–101

D.D. Bogard, P. Johnson, Science **221**, 651–654 (1983)

W.F. Bottke, J.C. Andrews-Hanna, Nat. Geosci. **10**, 344–348 (2017)

W.F. Bottke, M.D. Norman, Ann. Rev. Earth Planet. Sci. **45**, 619–647 (2017)

Bozlee, A. K. Misra, S. K. Sharma, and M. Ingram, Spectrochim. Acta. A Mol. Biomol. Spectrosc. **61** (2005)

A.J. Brown, S.J. Hook, A.M. Baldridge, J.K. Crowley, N.T. Bridges, B.J. Thomson, G.M. Marion, C.R. de Souza Filho, J.L. Bishop, Earth Planet. Sci. Lett. **297**, 174–182 (2010)

A.J. Brown, C.E. Viviano, T.A. Goudge, *J. Geophys. Res. Planets* **125** (2020)

T.E. Bunch, A.J. Cohen, M.R. Dence, Am. Miner. **52**, 244–253 (1967)

W.S. Cassata, D. Shuster, P.R. Renne, B.P. Weiss, Geochim. Cosmochim. Acta **74**, 6900–6920 (2010)

A.J. Cavosie, T.M. Erickson, N.E. Timms, S.M. Reddy, C. Talavera, S.D. Montalvo, M.R. Pincus, R.J. Gibbon, D. Moser, Geology **43**, 999–1002 (2015)

M. Chen, A. El Goresy, Earth Planet. Sci. Lett. **179**, 489–502 (2000)

B.A. Cohen, C.A. Malespin, K.A. Farley, P.E. Martin, Y. Cho, P.R. Mahaffy, Astrobiology **19**, 1303–1314 (2019)

B.A. Cohen, Geophys. Res. Lett. **33** (2006)

N. Dauphas, A. Pourmand, Nature **473**, 489–492 (2011)

V. Debaille, A.D. Brandon, Q.-Z. Yin, B. Jacobsen, Nature **450**, 525–528 (2007)

A. Deutsch, U. Schärer, Geochim. Cosmochim. Acta **54**, 3427–3434 (1990)

P.T. Doran, S.M. Clifford, S.L. Forman, L. Nyquist, D.A. Papanastassiou, B.W. Stewart, N.C. Sturchio, T.D. Swindle, T. Cerling, J. Kargel, G. McDonald, K. Nishiizumi, R. Poreda, J.W. Rice, K. Tanaka, Earth. Sci. Rev. **67** (2004)

B.L. Ehlmann, J.F. Mustard, C.I. Fassett, S.C. Schon, J.W. Head III., D.J. Des Marais, J.A. Grant, S.L. Murchie, Nat. Geosci. **1**, 355–358 (2008a)

B.L. Ehlmann, J.F. Mustard, S.L. Murchie, F. Poulet, J.L. Bishop, A.J. Brown, W.M. Calvin, R.N. Clark, Science **322**, 1828–1832 (2008b)

A. El Goresy, P. Gillet, M. Chen, F. Künstler, G. Graup, and V. Stähle, Am. Mineral. **86** (2001)

T.M. Erickson, N.E. Timms, C.L. Kirkland, E. Tohver, A.J. Cavosie, M.A. Pearce, S.M. Reddy, Contrib. Mineral. Petrol. **172**, 1–19 (2017)

K. Farley, C. Malespin, P. Mahaffy, J.P. Grotzinger, P.M. Vasconcelos, R.E. Milliken, M. Malin, K.S. Edgett, A. Pavlov, J.A. Hurowitz, J.A. Grant, Science **343**, 1247166 (2014)

K.A. Farley, K.H. Williford, K.M. Stack, R. Bhartia, A. Chen, M. de la Torre, K. Hand, Y. Goreva, C.D. Herd, R. Hueso, Y. Liu, Sp. Sci. Rev. **216**, 1–41 (2020)

A.C. Ferrari, J. Robertson, Phys. Rev. B **64**, 075414 (2001)

A.C. Ferrari, J. Robertson, Philos. Trans. R. Soc. Lond. A Math. Phys. Eng. Sci. **362**, 2477–2512 (2004)

L. Ferrière, G.R. Osinski (eds.), *Impact Cratering: Processes and Products* (Wiley, Chichester, 2013), pp. 106–124

J.J. Freeman, A. Wang, K.E. Kuebler, B.L. Jolliff, L.A. Haskin, Can. Mineral. **46**, 1477–1500 (2008)

B.M. French, in *Shock Metamorphism of Natural Materials*. ed. by B.M. French, N.M. Short (Mono Book Corp, Baltimore, 1968), pp. 383–411

B.M. French, *Traces of Catastrophe: A Handbook of Shock,* LPI Contribution No. 954 (1998)

L.R. Friedlander, T.D. Glotch, D.L. Bish, M.D. Dyar, T.G. Sharp, E.C. Sklute, J.R. Michalski, JGR: Planets **120**, 888–912 (2015)

J. Fritz, V. Assis Fernandes, A. Greshake, A. Holzwarth, U. Bottger, Meteorit. Planet. Sci. **54** (2019)

J. Fritz, A. Greshake, D. Stöffler, Antarct. Meteor. Res. **18**, 96 (2005)

P. Gavin, V. Chevrier, K. Ninagawa, A. Gucsik, S. Hasegawa, in *42th Lunar and Planetary Science Conference #1921* (2011)

C. Geiger, B.A. Kolesov, EMU Notes Mineral. **4**, 347–387 (2002)

D.I. Godfrey-Smith, D.J. Huntley, W.-H. Chen, Quat. Sci. Rev. **7**, 373–380 (1988)

J. Götze, M.R. Krbetschek, D. Habermann, D. Wolf, *in Cathodoluminescence in geosciences* (Springer, Berlin, 2000), pp. 245–270

T.A. Goudge, J.F. Mustard, J.W. Head, C.I. Fassett, S.M. Wiseman, JGR Planets **120**, 775–808 (2015)

T.A. Goudge, J.F. Mustard, J.W. Head, C.I. Fassett, JGR: Planets, **117**, 1–24 (2012)

M.M. Grady, Sp. Sci. Rev. **216**, 1–21 (2020)

A. Gucsik, C. Koeberl, F. Brandstätter, W.U. Reimold, E. Libowitzky, Earth Planet. Sci. Lett. **202**, 495–509 (2002)

H.C. Halls, Geophys. J. Int. **59**, 553–591 (1979)

J.P. Hamilton, M.R. Giles, P. Ainsworth, Geol. Soc. Lond. Spec. Publ. **61**, 377–400 (1992)

W.K. Hartmann, Meteorit. Planet. Sci. **34**, 167 (1999)

W.K. Hartmann, G. Neukum, *Chronology and Evolution of Mars* (Springer, Dordrecht, 2001), pp. 165–194

R.P. Harvey, M. Wadhwa, H.Y. McSween Jr., G. Crozaz, Geochim. Et Cosmochim. Acta **57**, 19 (1993)

L.A. Haskin, A. Wang, K.M. Rockow, B.L. Jolliff, K.M. Viskupic, JGR **102**, 19293–19306 (1997)

D. Heymann, F. Hörz, Phys Chem. Miner. **17**, 38 (1990)

L.L. Hood, N.C. Richmond, E. Pierazzo, P. Rochette, Geophys. Res. Lett. **30**, 14-1–14-4 (2003)

B.H.N. Horgan, R.B. Anderson, G. Dromart, E.S. Amador, M.S. Rice, Icarus **339**, 113526 (2020)

E. Huang, C.H. Chen, T. Huang, E.H. Lin, J. Xu, Am. Mineral. **85**, 473–479 (2000)

M. Humayun, A. Nemchin, B. Zanda, R.H. Hewins, M. Grange, A. Kennedy, J.-P. Lorand, C. Göpel, C. Fieni, S. Pont, D. Deldicque, Nature **503**, 513–516 (2013)

M. Jain, C.E. Andersen, L. Bøtter-Jensen, A.S. Murray, H. Haack, J.C. Bridges, Rad. Meas. **41**, 755–761 (2006)

B.M. Jakosky, M. Slipski, M. Benna, P. Mahaffy, M. Elrod, R. Yelle, S. Stone, N. Alsaeed, Science **355**, 1408–1410 (2017)

S.J. Jaret, L.C. Kah, R. Harris, Meteor. Plan. Sci. **49**, 1007–1022 (2014)

S.J. Jaret, W.R. Woerner, B.L. Phillips, L. Ehm, H. Nekvasil, S.P. Wright, T.D. Glotch, JGR Planets **120**, 570–587 (2015)

S.J. Jaret, J.R. Johnson, M. Sims, N. DiFrancesco, T.D. Glotch, GJR Planets **123**, 1701–1722 (2018a)

S.J. Jaret, S.R. Hemming, E.T. Rasbury, L.M. Thompson, T.D. Glotch, J. Ramezani, J.G. Spray, Earth Planet. Sci. Lett. **501**, 78–89 (2018b)

J.R. Johnson, Icarus **221**, 359–364 (2012)

J.R. Johnson, F. Hörz, P. Lucey, P.R. Christensen, JGR **107**, 3 (2002)

J.R. Johnson, F. Hörz, M.I. Staid, Amer. Mineral. **88**, 1575–1582 (2003)

J.R. Johnson, S.J. Jaret, T.D. Glotch, M. Sims, JGR Planets **125**, e2019JE006240 (2020)

J.R. Johnson and F. Hörz, JGR Planets **108** (2003)

F. Jourdan, Australian J. Earth Sci. **59**, 199–224 (2012)

F. Jourdan, P.R. Renne, W.U. Reimold, Earth Planet. Sci. Lett. **286**, 1–13 (2009)

F. Jourdan, F. Moynier, C. Koeberl, S. Eroglu, Geology **39**, 671–674 (2011)

H.R. Karlsson, R.N. Clayton, E.K. Gibson Jr., T.K. Mayeda, Science **255**, 1409–1411 (1992)

M. Kayama, T. Sekine, N. Tomioka, H. Nishido, Y. Kato, K. Ninagawa, T. Kobayashi, A. Yamaguchi, Meteorit. Planet. Sci. **53**, 1476–1488 (2018)

M. Kayama, H. Nishido, T. Sekine, T. Nakazato, A. Gucsik, K. Ninagawa, JGR Planets **117**, 1–13 (2012)

G.G. Kenny, L.F. Morales, J. Martin, J.A. Whitehouse, B. Petrus, S. Kamber, Geology **45**, 1003–1006 (2017)

G.G. Kenny, A. Karlsson, M. Schmieder, M.J. Whitehouse, A.A. Nemchin, J.J. Bellucci, Geology **48**, 19–23 (2020)

S.W. Kieffer, R.B. Schaal, R. Gibbons, R. Hörz, D.J. Milton, A. Dube, in *Lunar and Planetary Science Conference* (1976), pp. 1391–1412

F. Langenhorst, Bull. Czech Geol. Surv. **77**, 265–282 (2002)

C. Ma, O. Tschauner, J.R. Beckett, Y. Liu, G.R. Rossman, K. Zhuravlev, L.A. Taylor, Earth Planet. Sci. Lett. **422**, 194–205 (2015)

L. Mandon, C. Quantin-Nataf, P. Thollot, N. Mangold, L. Lozach, G. Dromart, P. Beck, E. Dehouck, S. Breton, C. Millot, M. Volat, Icarus **336**, 113436 (2020)

Mars Architecture Strategy Working Group (MASWG), Report by the NASA Mars Architecture Strategy Working Group (MASWG) (2020). https://mepag.jpl.nasa.gov/reports/MASWG%20NASA%20Final%20Report%202020.pdf

P.E. Martin, K.A. Farley, M.B. Baker, C.A. Malespin, S.P. Schwenzer, B.A. Cohen, P.R. Mahaffy, A.C. McAdam, D.W. Ming, P.M. Vasconcelos, R. Navarro-González, JGR: Planets **122**, 2803–2818 (2017)

S. Maurice, Wiens, R.C., Bernardi, P. Cais, et al. *Sp. Sci. Rev.* **217**, 1–108 (2021)

I. McDougall, T.M. Harrison, *Geochronology and Thermochronology by the 40Ar/39Ar Method*, 2nd edn. (Oxford University Press, Oxford, 1999)

M. McGregor, C.R.M. McFarlane, J.G. Spray, Earth Planet. Sci. Lett. **504**, 185–197 (2018)

D.A. McKeown, Am. Miner. **90**, 1506–1517 (2005)

S. McLennan, M. Sephton, D. Beaty, M. Hecht, B. Pepin, I. Leya, J. Jones, B. Weiss, M. Race, J. Rummel, K. Buxbaum, Astrobiology **12**, 175–230 (2012)

H.Y. McSween Jr., A. H. Treiman, in *Planetary Materials*. ed. by J.J. Papike (De Gruyter, Boston, 2018), pp. 953–1006

H.J. Melosh, *Impact Cratering: A Geologic Process* (Oxford University Press, Oxford, 1989)

T. Mernagh, J. Raman Spec. **22**(8), 453–457 (1991)

MEPAG ND-SAG, *Science Priorities for Mars Sample Return*, Unpublished white paper. (Mars Exploration Program Analysis Group, MEPAG, 2008). http://mepag.jpl.nasa.gov/reports/index.html. Accessed 1 Mar 2021

J.R. Michalski, T.D. Glotch, L.R. Friedlander, M.D. Dyar, D.L. Bish, T.G. Sharp, J. Carter, Geophys. Res. Lett. **44**, 6562–6569 (2017)

K. Mimura, M. Okamoto, K. Sugitani, S. Hashimoto, Meteorit. Planet. Sci. **42**, 347–355 (2007)

A.K. Misra, T.E. Acosta-Maeda, S.K. Sharma, C.P. McKay, P.J. Gasda, G.J. Taylor, P. Lucey, L. Flynn, M. Abedin, S. M. Clegg, Astrobiology **16** (2016)

A. Mittelholz, A. Morschhauser, C.L. Johnson, B. Langlais, R.J. Lillis, F. Vervelidou, B.P. Weiss, Earth Sp. Sci. **5**, 410–424 (2018)

S.M. Morrison, R.T. Downs, D.F. Blake, D.T. Vaniman, D.W. Ming, R. Hazen, A. Treiman, C.N. Achilles, A.S. Yen, R.V. Morris, E.B. Rampe, Am. Miner. J. Earth Planet. Mater. **103**, 857–871 (2018)

J.F. Mustard, M. Adler, A. Allwood, D.S. Bass, D.W. Beaty, J.F. Bell III, W.B. Brinckerhoff, M. Carr, D.J. Des Marais, B. Drake, K.S. Edgett, J. Eigenbrode, L.T. Elkins-Tanton, J.A. Grant, S.M. Milkovich, D. Ming, C. Moore, S. Murchie, T.C. Onstott, S.W. Ruff, M.A. Sephton, A. Steele, A. Treiman, Report of the Mars 2020 Science Definition Team, 154 pp. http://mepag.jpl.nasa.gov/reports/MEP/Mars_2020_SDT_Report_Final.pdf

NASA, *NASA-ESA Mars Sample Return Independent Review Board Report* (2020)

L.U. Nasdala, J.E. Götze, J.M. Hanchar, M.I. Gaft, M.R. Krbetschek, A. Beran, E. Libowitzky, Spec. Methods Miner. **6**, 43–91 (2004)

G. Neukum, B.A. Ivanov, W.K. Hartmann, in *Chronology and Evolution of Mars*. ed. by R. Kallenbach, J. Geiss, W.K. Hartmann (Springer, Dordrecht, 2001), p. 55

H.E. Newsom, N. Mangold, L.C. Kah, J.M. Williams, R.E. Arvidson, N. Stein, A.M. Ollila, J.C. Bridges, S.P. Schwenzer, P.L. King, J.A. Grant, P. Pinet, N. Bridges, N.F. Calef, III, R. Wiens, J. Spray, J.D. Vaniman, E.W. Elston, J. Berger, and C.M. Palucis, Icarus **249** (2015)

L.E. Nyquist, D. Bogard, C.-Y. Shih, J. Park, Y.D. Reese, A.J. Irving, Geochim. Cosmochim. Acta **73**, 4288–4309 (2009)

L.E Nyquist, F. Hörz, H. Wiesmann, C.-Y. Shih, B. Bansal, in *18th Lunar and Planetary Science Conference,* pp. 732–33 (1987)

E. Ohtani, Y. Kimura, M. Kimura, T. Kubo, T. Takata, Shock Waves **16**, 45–52 (2006)

R. Ostertag, JGR: Solid Earth **88**, B364–B376 (1983)

M. Ostroumov, E. Faulques, E. Lounejeva, C. R. Geosci. **334**, 21–26 (2002)

L. Pan, L., B. Ehlmann, P. Asimow, J. Hu, and R. Greenberger, in *49th Lunar and Planetary Science Conference* #1896 (2018)

J.D. Pasteris, O. Beyssac, Elements **16**, 87–92 (2020)

A.E. Pickersgill, R.L. Flemming, G.R. Osinski, Meteorit. Planet. Sci. **50**, 1851–1862 (2015)

A.E. Pickersgill, S.J. Jaret, L. Pittarello, J. Fritz, M. Harris, in *Large Meteorite Impacts and Planetary Evolution VI Series: GSA special papers.* ed. by W.U. Reimold, C. Koeberl (Geological Society of America, Glasgow, 2021), pp. 507–535

C.M. Pieters, P.A.J. Englert (eds.), *Topics in Remote Sensing 4. Remote Geochemical Analysis: Elemental and Mineralogical Composition* (Cambridge University Press, Cambridge, 1993)

C. Pieters, in *Lunar and Planetary Science Conference*, pp. 1031–1032 (1996)

L. Pittarello, J. Fritz, J. Roszjar, C. Lenz, N.C. Chanmuang, C. Koeberl, Meteorit. Planet. Sci. **55**, 669–678 (2020)

J. Pla-García, C.R. Rafkin, G.M. Martinez, Á. Vicente-Retortillo, C.E. Newman, H. Savijärvi, M. de la Torre, Sp. Sci. Rev. **216**, 1–21 (2020)

F. Poulet, J.P. Bibring, J.F. Mustard, A. Gendrin, N. Mangold, Y. Langevin, R.E. Arvidson, B. Gondet, C. Gomez, Nature **438**, 623–627 (2005)

E.B. Rampe, T.F. Bristow, R.V. Morris, S.M. Morrison, C.N. Achilles, D.W. Ming, D.T. Vaniman, D.T. Blake, V.M. Tu, S.J. Chipera, A.S. Yen, JGR: Planets **125** (2020)

J. Razzell Hollis, W. Abbey, L. Beegle, R. Bhartia, B.L. Ehlmann, J. Miura, B. Monacelli, K. Moore, A. Nordman, E. Scheller, Y.-H. Wu, PSS **209**, 105356 (2021)

J. Razzell Hollis, T. Fornaro, W. Rapin, J. Wade, A. Vicente-Retortillo, A. Steele, R. Bhartia, L.W. Beegle, Astrobiology **21**, 511–525 (2021)

M.P. Reitze, I. Weber, A. Morlok, H. Hiesinger, K.E. Bauch, A.N. Stojic, J. Helbert, Earth Planet. Sci. Lett. **554**, 116697 (2021)

B. Reznik, A. Kontny, J. Fritz, U. Gerhards, Geochem. Geophys. Geosyst. **17**, 2374–2393 (2016)

P. Rochette, G. Fillion, R. Ballou, F. Brunet, B. Ouladdiaf, L. Hood, Geophys. Res. Lett. **30**(1683), 16-1-16–4 (2003)

A.D. Rogers, N.H. Warner, M.P. Golombek, J.W. Head III., J.C. Cowart, Geophys. Res. Lett. **45**(4), 1767–1777 (2018)

L. Rubanenko, T.M. Powell, J.-P. Williams, I. Daubar, K.S. Edgett, D.A. Paige, in *Mars Geological Enigmas*. ed. by R.J. Soare, S.J. Conway, J.-P. Williams, D.Z. Oehler (Elsevier, Amsterdam, 2021), pp. 97–122

A.E. Rubin, Icarus **257**, 221–229 (2015)

U. Schärer, A. Deutsch, Geochim. Cosmochim. Acta **54**, 3435–3447 (1990)

M. Schmieder, D.A. Kring, Astrobiology **20**(1), 91–141 (2020)

S.C. Schon, J.W. Head, C.I. Fassett, Planet Space Sci. **67**(1), 28–45 (2012)

S.K. Shahrzad, K.M. Kinch, T.A. Goudge, C.I. Fassett, D.H. Needham, C. Quantin-Nataf, C.P. Knudsen, Geophys. Res. Lett. **46**, 2408–2416 (2019)

S.K. Sharma, B. Simons, H.S. Yoder, Am. Miner. **68**, 1113–1125 (1983)

T.G. Sharp, P.S. DeCarli, in *Meteorites and the Early Solar System*. ed. by D.S. Lauretta, H. McSween (University of Arizona Press, Tucson, 2006), pp. 653–677

S. Shkolyar, E. Eshelman, J.D. Farmer, D. Hamilton, M.G. Daly, C. Youngbull, Astrobiology **18**, 431–453 (2018)

S. Shkolyar, E. Lalla, M. Konstantindis, K. Cote, M.G. Daly, A. Steele, Icarus **354**, 114093 (2021)

M. Sims, S.J. Jaret, E.-R. Carl, B. Rhymer, N. Schrodt, V. Mohrholz, J. Smith, Z. Konopkova, H.-P. Liermann, T.D. Glotch, L. Ehm, Earth Planet. Sci. Lett. **507**, 166–174 (2019)

B.W. Smith, M.J. Aitken, E.J. Rhodes, P.D. Robinson, D.M. Geldard, Rad. Prot. Dosim. **17**, 229–233 (1986)

N.A. Spooner, Rad. Meas. **23**, 593–600 (1994)

K.M. Stack, N.R. Williams, F. Calef, the 2020 Science Team. *Sp. Sci. Rev.* **216**, 1–47 (2020)

D. Stoffler, JGR **76** (1971)

D. Stöffler, G. Ryder, in *Chronology and Evolution of Mars*. ed. by R. Kallenbach, J. Geiss, W.K. Hartmann (Springer, Dordrecht, 2001), p. 9

D. Stöffler, C. Hamann, K. Metzler, Meteorit. Planet. Sci. **53**(1), 5–49 (2018)

C. B. Stipe, E. Guevara, J. Brown, and G. R. Rossman, Spectrochim Acta Part B: At Spectrosc **70**, 45–50 (2012)

T.D. Swindle, A.H. Treiman, D.J. Lindstrom, M.K. Burkland, B.A. Cohen, J.A. Grier, B. Li, E.K. Olson, Meteorit. Plan. Sci. **35**, 107–115 (2000)

K.L. Tanaka, JGR: Solid Earth **91**, E139 (1986)

T. Tingle, J.A. Tyburczy, T.J. Ahrens, C.H. Becker, Orig. Life Evol. Biosph. **21**(5), 385–397 (1991)

E. Tohver, C. Lanna, P.A. Cawood, I.R. Fletcher, F. Jourdan, S. Sherlock, B.R.I. Trindade, E. Yokoyama, C.R. Souza Filho, Y. Marangoni, Geochim. Cosmochim. Acta **86**, 214–227 (2012)

I. Torre-Fdez, J. Aramendia, L. Gómez-Nubla, K. Castro, M. Maguregui, S. Fdez-Ortiz de Vallejuelo, G. Arana, J.M. Madariaga, Anal. Bioanal. Chem. **410**, 7477–7488 (2018)

G. Tschermak, Sitzber. Akad. Wiss. Wien. Math. Naturwiss. Kl. Abt. **I**(65), 122–146 (1872)

B. Velde, Y. Syono, M. Kikuchi, H. Boyer, Phys. Chem. Miner. **16**, 436–441 (1989)

E.L. Walton, S.P. Kelley, C.D.K. Herd, Geochim. Cosmochim. Acta **72**, 5819–5837 (2008)

E.L. Walton, S. Kelley, C.D.K. Herd, A.J. Irving, Geolog. Soc. Lond. Spec. Publ. **378**, 317–332 (2014)

A. Wang, K. Kuebler, B. Jolliff, L.A. Haskin, J. Raman Spec. **35**, 504–514 (2004a)

A. Wang, K. Kuebler, B. Jolliff, L.A. Haskin, Am. Miner. **89**, 665–680 (2004b)

P.H. Warren, Earth Planet. Sci. Lett. **311**, 93–100 (2011)

I. Weber, U. Böttger, S.G. Pavlov, E.K. Jessberger, H.-W. Hübers, Planet Space Sci. **104**, 163–172 (2014)

J.R. Weirich, T.D. Swindle, C.E. Isachsen, Meteorit. Planet. Sci. **47**(8), 1324–1335 (2012)

R.C. Wiens, R.O. Pepin, Geochim. Cosmochim. Acta **52**(2), 295–307 (1988)

R.C. Wiens, R.H. Becker, R.O. Pepin, Earth Planet. Sci. Lett. **77**, 149–158 (1986)

R.C. Wiens, S. Maurice, S.H. Robinson, A.E. Nelson, P. Cais, et al *Sp. Sci. Rev.* **217**, 1–87 (2021)

K.H. Williford, K.A. Farley, K.M. Stack, A.C. Allwood, D. Beaty, L.W. Beegle, R. Bhartia, A.J. Brown, M. de la Torre Juarez, S.E. Hamran, M.H. Hecht, *From Habitability to Life on Mars* (Elseiver, Amsterdam, 2018), pp. 275–308

T. Xie, G.R. Osinski, S.R. Shieh, Meteorit. Planet. Sci. **55**(7), 1471–1490 (2020)

Authors and Affiliations

S. Shkolyar[1,2,3] · **S. J. Jaret[4]** · **B. A. Cohen[2]** · **J. R. Johnson[5]** · **O. Beyssac[6]** · **J. M. Madariaga[7]** · **R. C. Wiens[8]** · **A. Ollila[8]** · **S. Holm-Alwmark[9,10,11]** · **Y. Liu[12]**

1   USRA, Columbia, MD, USA

2   NASA Goddard Space Flight Center, Greenbelt, MD, USA

3   Blue Marble Space Institute of Science, Seattle, WA, USA

4   American Museum of Natural History, New York, NY, USA

5   Applied Physics Laboratory, Johns Hopkins University, Baltimore, MD, USA

6   IMPMC, CNRS Sorbonne University, Paris, France

7   University of the Basque Country (UPV/EHU), Leioa, Spain

8   Los Alamos National Laboratory, Los Alamos, NM, USA

9   Niels Bohr Institute, University of Copenhagen, Copenhagen, Denmark

10   Natural History Museum Denmark, Copenhagen, Denmark

11   Lund University, Lund, Sweden

12   Jet Propulsion Laboratory, California Institute of Technology, Pasadena, CA, USA